Macromolecules

pubs.acs.org/Macromolecules Article

# Polymer Thin Film Necking: Ductility from Entanglements and Plane Stress Condition

Siteng Zhang, Zhiqiang Cao, Xiaodan Gu, and Ting Ge*

Cite This: *Macromolecules* 2024, 57, 6221−6232 Read Online

ACCESS | Metrics & More | Article Recommendations | Supporting Information

**ABSTRACT:** The ductility of polymer thin films is critical to many applications such as organic electronics and separation membranes. Large-scale molecular simulations are performed to reproduce the experimentally observed necking, a ductile deformation mode. The simulations show that the morphology of a necked film differs qualitatively from craze fibrils in brittle polymers. The micromechanics of thin film necking are revealed with details transcending the capability of experiments. The free boundary of a thin film promotes the plane stress condition and allows the onset of a neck via strain localization. The underlying entanglement network stabilizes the neck by preventing chain pullout. The strain hardening of entangled polymers in the neck region compensates for the reduction in thickness and supports stable neck propagation under a constant tensile force with no bond breaking. Despite the critical role of entanglements, the width of the neck is much larger than the entanglement spacing. The Considère construction predicts well the onset of necking but not the draw ratio of necked polymers, where voids break down the conservation of volume. Krupenkin and Fredrickson's geometric argument based on the extension of entanglement network strands is able to predict the draw ratio, as verified by the topological analysis using the Z1+ package. The ductile thin film necking is consistently observed in the simulations with thicknesses larger than the unperturbed polymer chain size, temperatures below the glass transition, and deformation rates much higher than the limited monomer mobility.

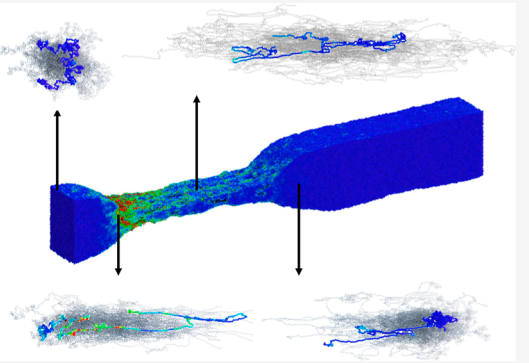



## 1. INTRODUCTION

Recent advances in nanoengineering have enabled sub-100 nm polymer thin films to be fabricated and thus propelled their applications in organic electronics, coating, filtration, and separation technologies.[1−14] Many functions of polymer thin films rely on their high strength-to-weight ratio and durability, both highlighting the significance of their mechanical properties. One particularly intriguing observation is that a brittle polymer glass in the bulk state, such as polystyrene (PS), exhibits ductility in the thin film state via the shear deformation resulting from necking.[6,12,14] This brings film thickness as a new dimension to the parameter space determining the brittle-to-ductile transition, which is a central topic in glassy polymer mechanics.[15−20] The microscopic mechanism of ductile thin film necking needs to be understood to promote the rational molecular design of stretchable and durable polymer thin films.

Molecular simulations have offered unique insights into various mechanical processes in glassy polymers[21−35] and may also be used to study necking. This work establishes protocols for reproducing the experimentally observed thin film necking in large-scale molecular simulations. The system parameters are properly chosen to target the necking process with the nanoconfinement effects in ultrathin films[6,12,14] excluded. The simulations demonstrate that ductile necking relies on an entanglement network that stabilizes the neck formed under the plane stress conditions and subsequently supports the propagation of the neck at a constant tensile force. The simulations reveal the changes in thin film morphology, the distributions of local strain and stress, the evolution of chain conformations during necking, and the spatial variations of entanglement density, all of which are experimentally hard to study but essential aspects of micromechanics. Section 2 describes the model and methods for simulations of polymer thin film necking. Section 3 provides details of the experiments. Section 4 reports the results of the molecular simulations and the experiments. The paper concludes with Section 5, where key results are summarized.

## 2. SIMULATION MODEL AND METHODS

The generic coarse-grained bead−spring model[36] is employed in the simulations. All beads of size $a$ and mass $m$ interact via the pairwise 12−6 Lennard-Jones (LJ) potential that is truncated at $r_c$. The interaction strength of the LJ potential is $\varepsilon$. Adjacent beads along a polymer chain are connected by the finite extensible nonlinear elastic (FENE) potential. A polymer thin film containing $M$ chains, each of which

Received: March 22, 2024
Revised: May 24, 2024
Accepted: May 31, 2024
Published: June 17, 2024

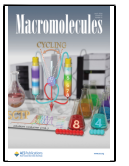





https://doi.org/10.1021/acs.macromol.4c00656
*Macromolecules* 2024, 57, 6221−6232

consists of $N$ beads, was constructed by generating random-walk coils between two confining walls. The two walls were separated by a distance of $94.3a$ along the $x$-direction and interacting with the monomers via the 9−3 LJ potential. Periodic boundary conditions were applied in the $yz$-plane with box sizes of $L_y = 61.7a$ and $L_z = 185.2a$. The box dimensions were chosen such that the number density of monomers $\rho = 0.85a^{-3}$ and the film thickness are multiple times the unperturbed average end-to-end chain size. Five thin film samples of $N$ = 50, 100, 160, 200, and 500 were simulated with $M$ = 18 000, 9000, 5625, 4500, and 1800, respectively. Moreover, a larger sample with $N$ = 500, $M$ = 3600, and $L_z$ doubled to $370.4a$ was simulated.

For the polymer model used here, the entanglement length $N_e \approx 80$.[37,38] This value corresponds to the "rheological" entanglements that determine the plateau modulus in the melt state. The "topological" entanglements that enter the construction of the primitive paths are about twice more dense.[39] Application of the state-of-the-art Z1+ package for entanglement analysis identifies that the average length between kinks along a primitive path is $N_k \approx 40 \approx N_e/2$ for the model used. The exact value of $N_e$ extracted from the statistics of primitive paths depends on the treatment of finite chain size effects as well as the use of different estimators.[37]

All samples were equilibrated thoroughly with $r_c = 1.12a$ at temperature $T = 1.0\varepsilon/k_B$. The temperature was maintained by a Nosé−Hoover thermostat with a characteristic damping time $1\tau = 1a\sqrt{m/\varepsilon}$. The time step for integrating the equations of motion was $\delta t = 0.005\tau$. To accelerate the equilibration, pairs of nearby bonds may be swapped using the Monte Carlo rules with the Boltzmann acceptance criterion.[40] The bond-swapping process permits the crossing of polymer chains and speeds up the chain dynamics with respect to the slow entangled dynamics, where the chains cannot cross each other. This acceleration algorithm is known as "double bridging" and realized by the "fix bond/swap" command in the LAMMPS package.[41] Figure 1 shows $C_n = \langle R_{ee}^2(n)\rangle/nl_0^2$ for the thin film with $N$ = 500 and $M$ = 3600, where $\langle R_{ee}^2(n)\rangle$ is the root-mean-square (RMS) end-to-end size of a chain section of $n$ consecutive bonds and $l_0 = 0.96a$ is the average FENE bond length. Also shown in Figure 1 are the three components $C_{n,i} = \langle R_{ee,i}^2(n)\rangle/nl_0^2$, where $i = x$, $y$, or $z$. $C_n$ increases with $n$ and eventually approaches the characteristic ratio of 1.8. Moreover, the three components $C_{n,x}$, $C_{n,y}$, and $C_{n,z}$ are almost the same. This indicates that the confining walls in the $x$-direction have not perturbed the isotropic chain conformations, as the film thickness $94.3a$ is larger than the average chain size $\langle R_{ee}^2(n = 499)\rangle^{1/2} = 28.8a$. The equilibrated melt samples were quenched with $r_c = 1.5a$ to the glassy state at $T = 0.1\varepsilon/k_B$, which is below the glass transition temperature $T_g \approx 0.32\varepsilon/k_B$. Details of the quenching simulation and the determination of $T_g$ are in the Supporting Information. The cutoff $r_c = 1.5a$ balances the need to include the attractive tail of the LJ potential and the computational cost, as used in previous simulations.[21−23,26,28−30,33]

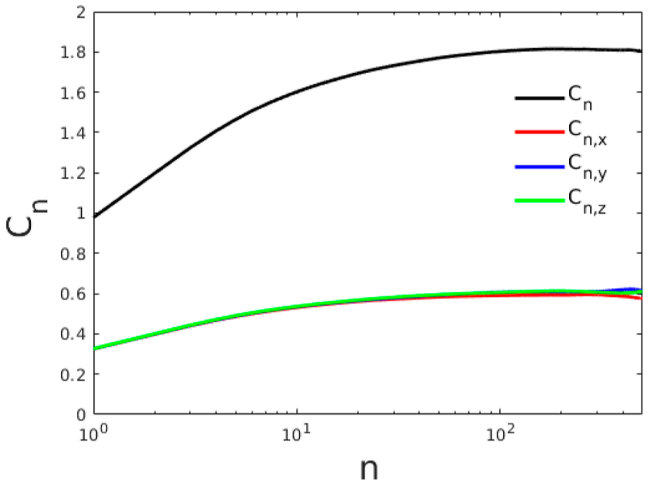


**Figure 1.** $C_n = \langle R_{ee}^2(n)\rangle/nl_0^2$ and its three components for the equilibrated thin film of $N$ = 500 and $M$ = 3600 at $T = 1.0\varepsilon/k_B$.

The mechanical test on a glassy polymer thin film was conducted by stretching it along the $z$-direction at a constant velocity $v_0 = 0.04a/\tau$, which is in the regime where stress depends weakly on strain rate.[42] The confining walls for equilibrating and quenching the thin film in the melt state were removed during the stretching; as such, there was a free boundary condition in the $x$-direction. There is no need to keep the confining walls, as free boundaries of the glassy thin film with limited monomer mobility are stable without external deformation. The glassy polymers could contract in the $x$-direction, while $L_y$ in the periodic $y$-direction remained unchanged. Thus, a plane stress condition was created with stress vanishing in the $x$-direction. During the stretching, a Langevin thermostat with $T = 0.1\varepsilon/k_B$ and a characteristic damping time of $1\tau$ was applied only to the $y$-direction.

A stress tensor is associated with each atom. The symmetric stress tensor has 6 independent components $S_{ij}$ with $ij = xx, yy, zz, xy, xz$, and $yz$. The tensile stress component

$$S_{zz} = -[mv_z^2 + \Sigma_{n=1}^{N_{LJ}}(z_1^{LJ}f_{z,1}^{LJ} + z_2^{LJ}f_{z,2}^{LJ})/2 + \Sigma_{n=1}^{N_{FENE}}(z_1^{FENE}f_{z,1}^{FENE} + z_2^{FENE}f_{z,2}^{FENE})/2] \quad (1)$$

where the first term is a kinetic energy contribution from the $z$-component $v_z$ of the instantaneous velocity of the atom, $z_1^{LJ/FENE}$ and $z_2^{LJ/FENE}$ are the $z$-coordinates of the two atoms interacting via the LJ/FENE potential, $f_{z,1}^{LJ/FENE}$ and $f_{z,2}^{LJ/FENE}$ are the $z$-components of the corresponding forces in the virial terms, and $N^{LJ/FENE}$ are the numbers of LJ/FENE interactions involving the atom analyzed. To compute the nominal tensile stress for a deformed thin film, the sample is divided into slices lying in the $xy$-plane, which is normal to the $z$-direction for the stretching. The width of a slice is $1a$. The $z$-component of the true stress $\sigma_{local}(z)$ in each slice is calculated as the sum of $S_{zz}$ for all atoms in the slice divided by the volume of the slice. $\sigma_{local}(z)$ is at its lowest value in the thickest slice, corresponding to the grip force in a dog-bone tensile test. As a result, $\sigma_{local}(z)$ in the thickest slice is determined as the nominal tensile stress $\sigma_n$. All simulations were performed using the LAMMPS package.[41]

## 3. EXPERIMENT DETAILS

Polystyrene (number-averaged molecular weight $M_n$ = 173 kDa, dispersity = 1.06) was purchased from Polymer Source and used as received. Poly(sodium 4-styrenesulfonate) (PSS) was purchased from Sigma-Aldrich and used as received. Polystyrene solution (20 mg/mL in toluene) was spun-cast on the Si substrate covered with a water-soluble PSS layer (≈30 nm) to form a bilayer composite film structure with a PS film of 84.7 nm thick (from the atomic force microscopy (AFM) measurement of the step height between the PS film and bare silicon wafer). Then, the polymer film was laser etched into a dog-bone shape. The dog-bone-shaped film (2 mm in width and 8 mm in length) was floated onto water, followed by careful lowering of two aluminum tensile grips coated with a thin layer of polydimethylsiloxane (PDMS) (approximately 0.5 mm). The polymer film was securely bonded to the PDMS pads through van der Waals forces.

The thin film tensile test was performed by a pseudo free-standing tensile test method. In the test, the strain of the thin film was applied via a motorized linear stage equipped with a digital encoder (Micronix Inc.), while the force exerted on the film was monitored using a high-resolution load cell (KYOWA Inc.). Stress−strain curve was derived from the force−displacement curve, with stress calculated as the force divided by the cross-sectional area of the thin film. The strain was determined by measuring the displacement in the sample length relative to the original length of the film. More details of the


https://doi.org/10.1021/acs.macromol.4c00656
Macromolecules 2024, 57, 6221−6232

pseudo free-standing tensile test method are presented in our previous publications.[9,13] The stretched film was transferred to a silicon substrate for the ZEISS microscope. AFM image was obtained on an Asylum Research Cypher S AFM in tapping mode. The film was transferred to the top of the flat silicon substrate for AFM. The height of the shear deformation zone is measured by the step height between the shear deformation zone and the substrate.

## 4. RESULTS

**4.1. Stress−Stretch Curve and Neck Profile.** The nominal stress $\sigma_n$ as a function of the stretch ratio $\lambda = L_z/L_z^0$, where $L_z^0$ is the length of the film in the $z$-direction prior to the stretching, depends on $N$ with respect to $N_e \approx 80$. As shown in Figure 2a, the initial elastic stress rise, the yielding, and the subsequent stress drop due to strain localization are all independent of $N$. However, there is a remarkable $N$-dependence of the mechanical response upon a larger deformation. For the shortest $N = 50 < N_e$, $\sigma_n$ continues to drop to zero with increasing $\lambda$. Accordingly, the film fails at the point of strain localization via chain pullout, as illustrated by the side profiles of the film in Figure 2b. With increasing $N$, the stress drop is delayed to a larger $\lambda$. For $N = 160 = 2N_e$, the failure mode of the film is still chain pullout. However, for $N = 200$ and 500 above $2N_e$, there is a plateau in the stress−stretch curve. In the plateau regime, the initial strain localization is stabilized and a neck propagates throughout the sample steadily, as illustrated by the side profiles for $N = 500$ in Figure 2c. After the plateau ends, $\sigma_n$ rises again, corresponding to further stretching of the completely necked film. In short, Figure 2 demonstrates that the entanglements in long polymer chains with $N > 2N_e$ act to prevent catastrophic chain pullout, providing a necessary foundation for necking. Movies of stable thin film necking in the simulations are provided in the Supporting Information.

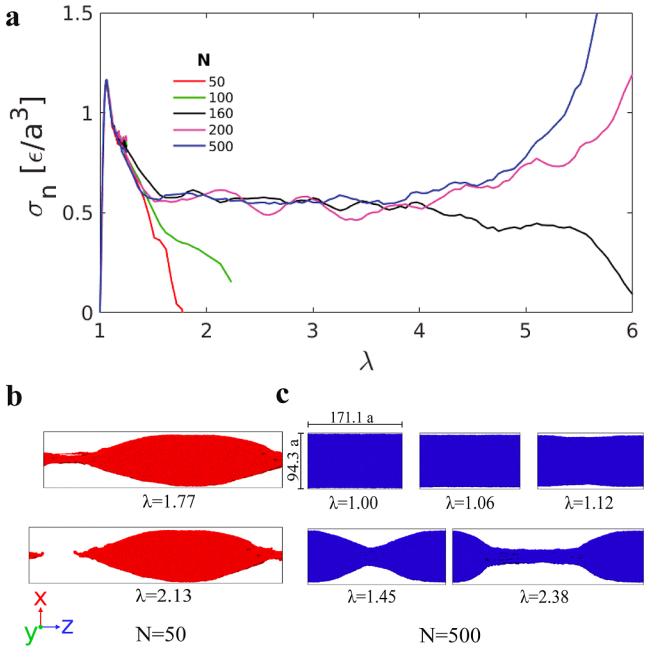


**Figure 2.** (a) Nominal tensile stress $\sigma_n$ as a function of the stretch ratio $\lambda$ for the glassy polymer thin films of indicated chain length $N$. Side profiles of the thin films of $N = 50$ and 500 during the mechanical test are shown in (b,c), respectively.

Using the pseudo free-standing tensile tester,[43] the necking in a sub-100 nm thin film made of well-entangled ($N \approx 10N_e$) PS is observed. As shown in Figure 3, shear deformation zones (SDZs) of reduced thickness alternate with thicker regions along the direction of tensile loading. The engineering stress−strain curve in Figure 3c exhibits a global failure strain of about 12%, indicating the necking-induced ductility. While the local stress−strain behavior is not experimentally tractable, the AFM enables a measurement of the local variation in the film thickness. Figure 3d shows that the film thickness is reduced from the original 84.7 to 16.5 nm in the SDZ. Comparing the simulations and experiments, one sees that local necking in the experiments is reproduced well by the simulations. Note that, using $a \approx 0.76$ nm for PS,[39] the film thickness 94.3$a$ in the simulations may be mapped to 72 nm, which is comparable to the thickness in the experiment.

**4.2. Morphology and Micromechanics of Necking.** More aspects of thin film necking, which are difficult if not impossible to study experimentally, are examined by the simulations. As shown in Figure 4a for the thin film with $N = 500$ and $M = 3600$, a neck exists between a thick $\alpha$ region and a thin $\beta$ region during stable necking. The colored contour plot of the von Mises local shear strain invariant $\varepsilon_v$ over a global increment $\delta\lambda = 0.05$ indicates that the neck is the region of large nonvanishing local strain (see Supporting Information for the calculation details). The cross sections at different locations of the neck depict the changes in the thin film morphology during necking. The scattered cavitation in the neck renders a thin film perforated with voids in the $\beta$ region. Because of the voids, the density of monomers in the $\beta$ region is reduced to $\rho^\beta \approx 0.75a^{-3}$ with respect to the density $\rho^\alpha \approx 1.0a^{-3}$ in the $\alpha$ region, as seen in the density profile in Figure 4b. In experiments, transmission electron microscopy of the fractured PS thin film of thickness 80 nm showed no clear voids in the SDZ far from the crack tip but noticeable voids in those near the crack tip.[12]

The morphology of the $\beta$ region differs distinctively from that induced by crazing, which is a brittle failure mode of glassy polymers under tensile loading.[21,22,44−47] As shown by previous simulations[21,22,33,46,47] as well as the simulations and movie in Supporting Information, crazing leads to a forest of fibrils with voids between them. The replacement of crazing by necking in the simulations arises from changes in the boundary conditions in the plane normal to the stretching direction. While crazing relies on both directions in the plane being periodic, necking requires one direction to be free. This difference in boundary conditions corresponds to contrasting stress conditions: triaxial stress for crazing whereas plane stress for necking. For the experiments shown in Figure 3, the plane stress condition is facilitated by the sub-100 nm thickness of the PS film. Additional experiments of thicker PS films of thickness above 200 nm show that no necking-induced SDZs may be observed, indicating the difficulty in producing the plane stress condition as films become more bulk-like.

By visual inspection, the neck region in Figure 4a is wider than the entanglement spacing $d_e \approx 8a$, which corresponds to the RMS end-to-end size of a strand consisting of $N_K = 40$ monomers between kinks along the primitive path. An analytic solution of the neck profile has been derived,[48] which may be simplified to an exponentially decaying profile as in a liquid jet, but it does not capture the smooth joint between the neck and the $\alpha$ region. Without a theory-informed function, one could alternatively fit the neck profile to an empirical function. Figure S4 in Supporting Information shows the thickness profile of the


https://doi.org/10.1021/acs.macromol.4c00656
Macromolecules 2024, 57, 6221−6232

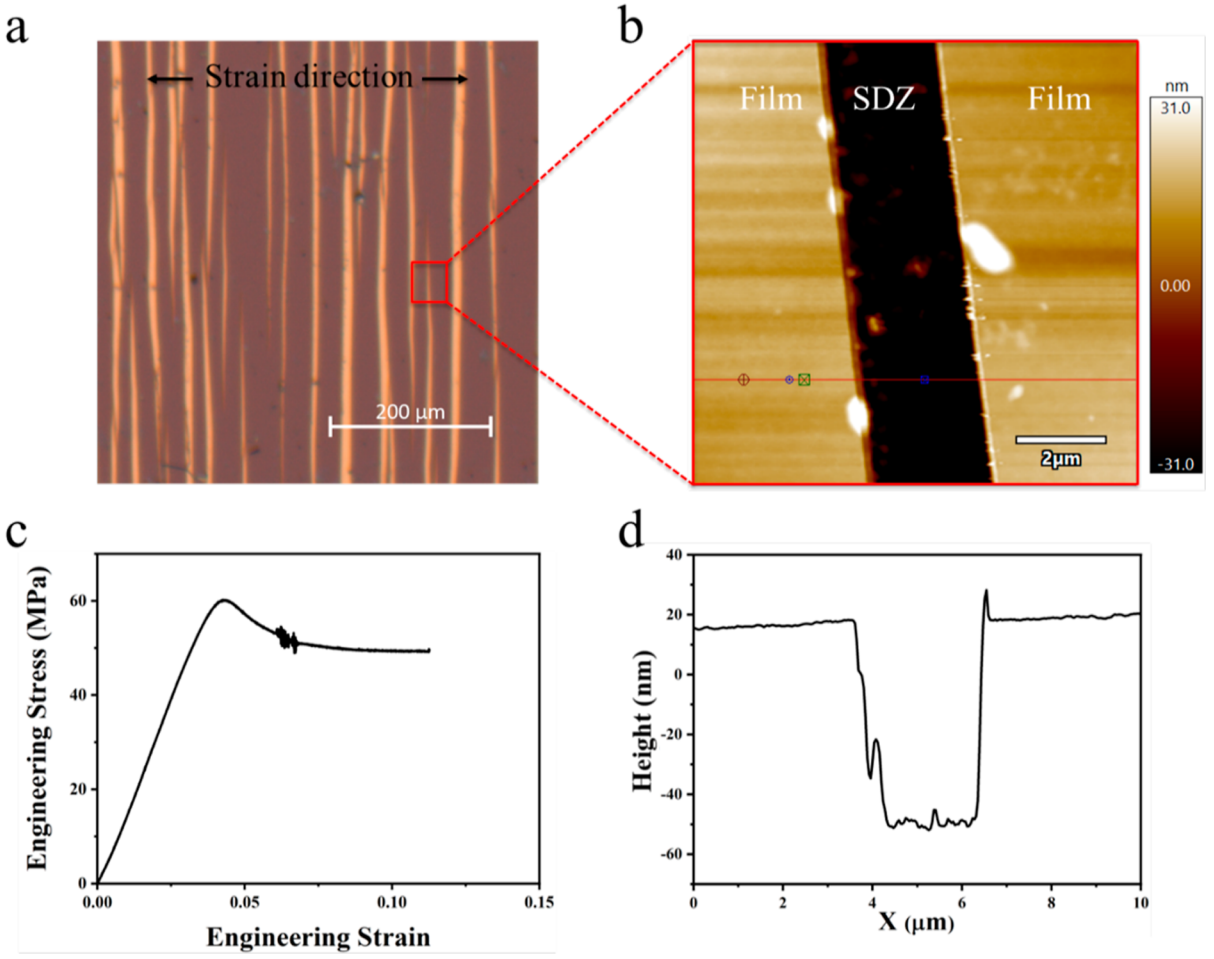


**Figure 3.** (a) Optical image of the stretched PS thin film sitting on a silicon wafer. (b) AFM 2D height image showing the boundary between a SDZ and the rest of the film. (c) Engineering stress−strain curve from the tensile test. (d) 1D line cut showing the film thickness along the sample.

film in Figure 4 is fit well by $h(z) = \Delta h \tanh[(z - z_0)/w] + h_0$, where $z_0$, $h_0$, $w$, and $\Delta h$ are the fitting parameters indicating the center of the neck, the film thickness at the center, the width, and the thickness variation with respect to the center, respectively. The best fit result is $w = 31.4a$. The region of width $2w = 63a$ around the neck center is indicated in Figure 4a. Such a region is much wider than $d_e$, in contrast to the active zone width in crazing being comparable to $d_e$ (see Figures S3 and S4 for a comparison).

The propagation of the neck along the stretching direction occurs under a constant tensile force. Figure 4c shows that the local tensile stress $\sigma_{local}(z)$ is higher in the $\beta$ region than in the $\alpha$ region. There is a gradual decrease in the $\sigma_{local}(z)$ across the neck, which is commensurate with the thickness profile. The product of $\sigma_{local}(z)$ and the cross-sectional area $A(z) = h(z)L_y$ in the $xy$-plane is local tensile force $f(z)$. Figure 4e shows that a constant tensile force is relayed from the $\alpha$ region through the neck to the $\beta$ region.

The dominant contribution to $\sigma_{local}(z)$ is from the LJ potential in the $\alpha$ region but is from the FENE potential in the $\beta$ region. This is revealed by the decomposition of $\sigma_{local}(z)$ to $\sigma^{LJ}(z)$ and $\sigma^{FENE}(z)$ in Figure 4d. The kinetic energy contribution to $\sigma(z)$ is minor in the glassy state and hence is not shown. From the $\alpha$ region to the $\beta$ region, the stress carried by intermolecular LJ interactions only slightly decreases due to the small reduction in $\rho$. By contrast, the stress carried by intramolecular bonds significantly increases and raises the total stress. Further calculations on the statistics of bond length show that the average bond length does not change much during necking, although the probability distribution function becomes wider (see Figure S5). These results suggest that the entanglement network forces the chain conformations to adapt to the necking profile without inducing much average bond tension along the chain backbone.

To further demonstrate that bond breaking does not play a role in thin film necking, an additional simulation with breakable quartic bonding potential[21,49] was performed. The quartic bonds have the same equilibrium length as the FENE bonds. However, unlike FENE bonds with tension diverging at large extension, the quartic bonds break with vanishing bond tension at large extension. Quartic bonds have been shown to capture the bond-breaking behavior in glassy polymer mechanics. If bond breaking played a role in thin film necking, it would emerge in the alternative simulation with quartic bonds. As shown in Figure 5, stretching the same thin film as in Figure 4, but with the FENE bonds replaced by the quartic bonds, gives a similar stress−stretch curve. The yield stress and the plateau drawing stress for neck propagation are observed for the quartic bonds (Figure 5a), although their values are lower than those for the FENE bonds. Moreover, the necked thin film with the quartic bonds exhibits a similar morphology as the film in Figure 4. One sees the coexistence of the $\alpha$ and $\beta$ regions during necking propagation (Figure 5b). Further examination of the quartic bonds shows that none of the bonds have broken during the


https://doi.org/10.1021/acs.macromol.4c00656
Macromolecules 2024, 57, 6221−6232

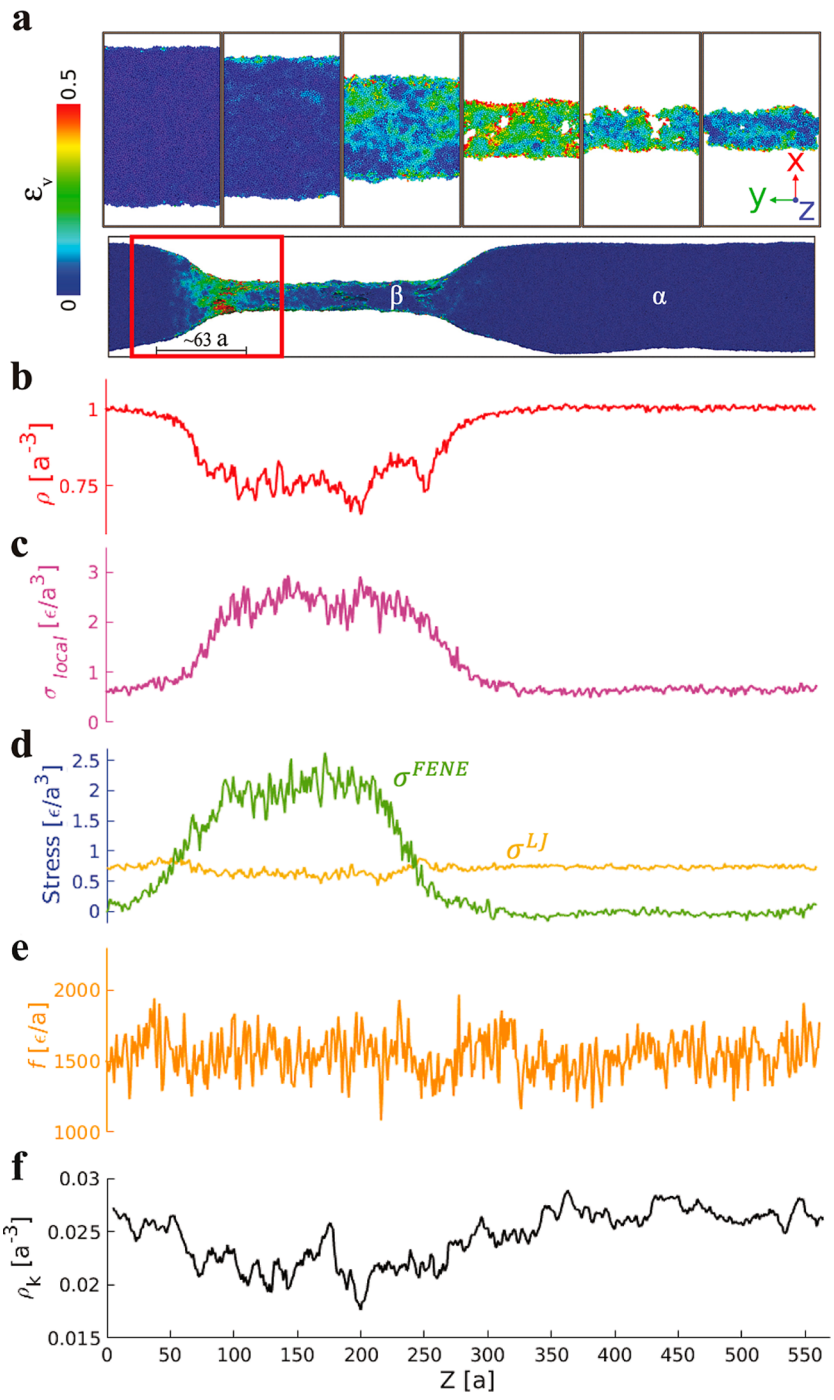


**Figure 4.** (a) Side profile and selected cross sections of the glassy polymer thin film with $N = 500$ and $M = 3600$ at $\lambda = 1.5$ during necking. Colors indicate the von Mises local shear strain invariant $\varepsilon_v$. Cross sections are evenly selected from the region indicated by the red box overlaid on the side profile. Each cross-section lying in the $xy$-plane is of width $5a$ along the $z$-direction. Profiles of the (b) monomer number density $\rho$, (c) local tensile stress $\sigma_{local}$, (d) two stress components $\sigma^{LJ}$ and $\sigma^{FENE}$, (e) tensile force $f$, and (f) kink number density $\rho_k$ as functions of $z$, all corresponding to (a).

necking process. As a result, it is concluded that thin film necking does not require bond breaking, which justifies the use of unbreakable FENE bonds in the simulations.

**4.3. Chain Conformations and Draw Ratio.** The contrasting conformations of polymer chains in the $\alpha$ and $\beta$ regions are illustrated in Figure 6a. In the $\alpha$ region, the mean values of the three components of the radius of gyration are $R^{\alpha}_{g,x} = (4.6 \pm 0.1)a$, $R^{\alpha}_{g,y} = (5.0 \pm 0.1)a$, and $R^{\alpha}_{g,z} = (5.4 \pm 0.1)a$. Compared to the undeformed state with $R^{0}_{g,x} = R^{0}_{g,y} = R^{0}_{g,z} = 5.0a$, the chains in the $\alpha$ region are slightly stretched by $\lambda^{\alpha} = R^{\alpha}_{g,z}/R^{0}_{g,z} = 1.08 \pm 0.02$ in the $z$-direction while slightly compressed by $\kappa^{\alpha} = R^{\alpha}_{g,x}/R^{0}_{g,x} = 0.92 \pm 0.02$ in the $x$-direction. In the $\beta$ region, $R^{\beta}_{g,x} = (1.30 \pm 0.04)a$, $R^{\beta}_{g,y} = (5.2 \pm 0.2)a$, and $R^{\beta}_{g,z} = (26.8 \pm 1.1)a$, corresponding to larger deformation with $\lambda^{\beta} = R^{\beta}_{g,z}/R^{0}_{g,z} = 5.4 \pm 0.2$ and $\kappa^{\beta} = R^{\beta}_{g,x}/R^{0}_{g,x} = 0.26 \pm 0.01$.

The draw ratio of polymer chains during necking is predicted by the Considère's construction.[16] Based on a constant $z$-independent tensile force $df(z)/dz = 0$ and the conservation of polymer volume $d[A(z)\lambda(z)]/dz = 0$, Considère determined $d\sigma(z)/d\lambda(z) = \sigma(z)/\lambda(z)$ needs to be satisfied both in the $\alpha$ and


https://doi.org/10.1021/acs.macromol.4c00656
Macromolecules 2024, 57, 6221−6232

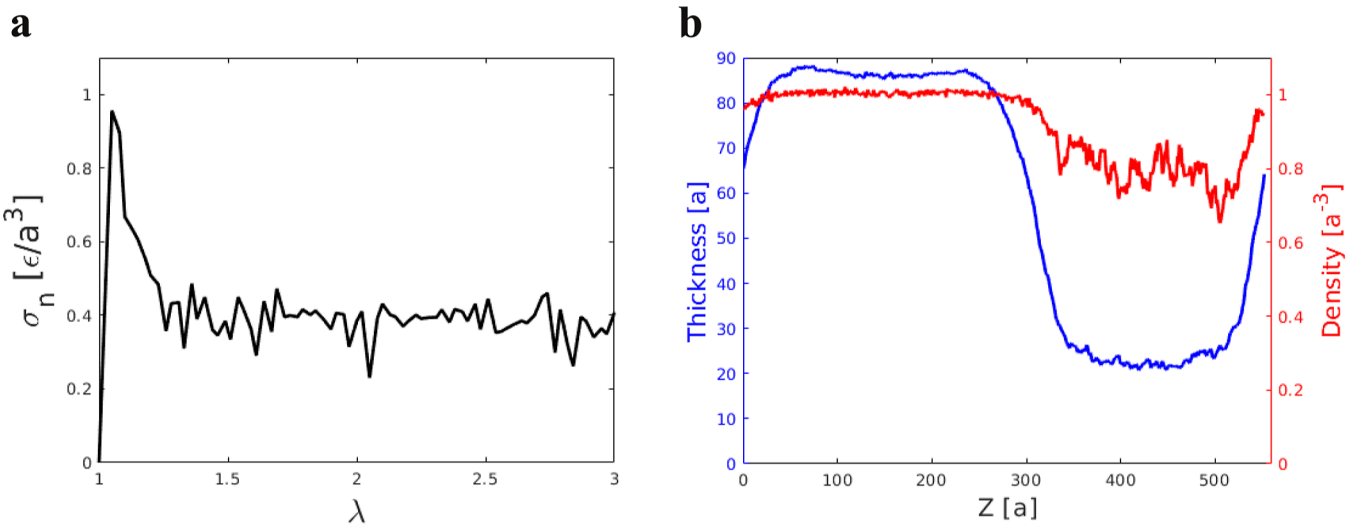


**Figure 5.** (a) Nominal tensile stress $\sigma_n$ as a function of the stretch ratio $\lambda$ and (b) the thickness (blue line) and density profiles (red line) from the necking of the thin film of $N = 500$ and $M = 3500$ with breakable quartic bonds.

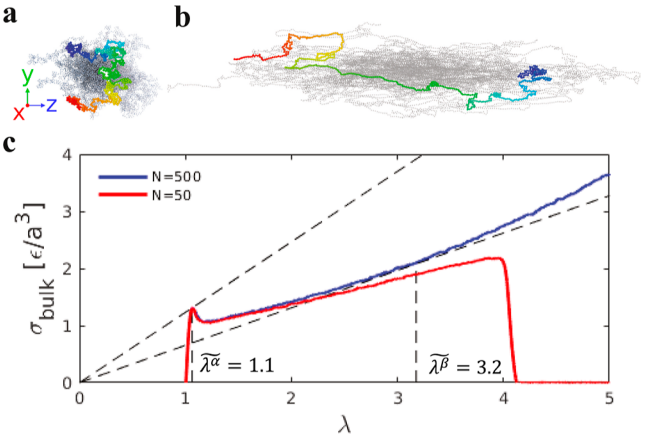


**Figure 6.** Snapshots of polymer chains in the (a) $\alpha$ and (b) $\beta$ regions. The gray cloud indicates multiple chains with overlapping center-of-mass positions, while a chain with its radius of gyration close to the ensemble average is highlighted with the rainbow color along the chain contour. (c) Tensile stress $\sigma_{bulk}$ as a function of $\lambda$ for the two bulk samples of $N = 500$ and 50. Dashed lines indicate the Considère's construction.

$\beta$ regions. Accordingly, one needs to identify the points on the stress−stretch curve with their local tangent lines going through the origin. To use Considère's construction, the intrinsic stress−stretch curve of the simulated polymer in the bulk state is needed. Two bulk samples of $N = 500$ and $N = 50$ were prepared, and their glassy mechanics were simulated. Details of the simulations are listed in Supporting Information.

The tensile stress $\sigma_{bulk}$ in the $z$-direction as a function of $\lambda$ for the two bulk samples is shown in Figure 6c. For $N = 500$, there is sufficient strain hardening at large $\lambda$, and the Considère's construction, as indicated by the dashed lines, predicts that a neck forms at $\tilde{\lambda}^{\alpha} = 1.1$ and stabilizes at $\tilde{\lambda}^{\beta} = 3.2$. For $N = 50$, strain hardening is weaker at large $\lambda$, and the sample ultimately fails through chain pullout. As a result, only the dashed line that gives $\tilde{\lambda}^{\alpha} = 1.1$ may be constructed, and no stable necking is predicted. The Considère's construction successfully predicts the onset of stable necking with increasing $N$ in Figure 2. It also captures one necessary condition for stable necking: sufficient strain hardening in the $\beta$ region that compensates for the thickness reduction. Quantitatively, the predicted draw ratio $\tilde{\lambda}^{\beta}$ is smaller than $\lambda^{\beta}$ in the simulations. Unlike the assumption by Considère, the formation of voids during necking in the simulations (Figure 4) increases the polymer volume, leading to the breakdown of Considère's criterion for the $\beta$ region.

A simple geometric argument developed by Krupenkin and Fredrickson[48] bypasses the micromechanics and relates the draw ratio $\lambda^{\beta}$ in necking to the extension of the entanglement network strands. The argument is evaluated here by a topological analysis of entanglements in the simulations. The entanglement network in the necked film with coexisting $\alpha$ and $\beta$ regions in Figure 4 is analyzed using the Z1+ package, which identifies kinks along the primitive paths of polymer chains.[38] Figure 4f shows the kink number density $\rho_K$ as a function of $z$ along the stretching direction. $\rho_K^{\beta}$ in the necked $\beta$ region is lower than $\rho_K^{\alpha}$ in the $\alpha$ region, correlating with the reduction of the monomer number density $\rho^{\beta}$ with respect to $\rho^{\alpha}$. The ratio $\rho_K/\rho$ is equivalent to the number of monomers between adjacent kinks $N_K$. For the thin film in Figure 4, $N_K = \rho_K/\rho = 37.5 \pm 2.3$, which is almost constant independent of $z$. According to Krupenkin and Fredrickson, an entanglement strand is in Gaussian random-walk coil conformation before necking, whereas in the necked region, it only retains the random-walk conformation in one direction: the direction within the thin film plane but normal to the stretching direction, i.e., the periodic $y$-direction in Figure 4. Meanwhile, the contour length stored in the other two directions, i.e., the $x$- and $z$-directions in Figure 4, is pulled taunt and aligned along the $z$-direction. Using the strands between kinks from the Z1+ analysis as representations of entanglement strands, one can use Krupenkin and Fredrickson's argument to numerically predict $\lambda^{\beta}$. The strand length along the $z$-direction in the necked region is $d_{K,z} = (2/3)l_0N_K = (2/3) \times 0.96a \times 38 = 24.3a$, where the prefactor 2/3 arises from the conformation changes in 2 out of 3 orthogonal directions of a random-walk coil. The RMS end-to-end size of the same strand along the $z$-direction is


https://doi.org/10.1021/acs.macromol.4c00656
Macromolecules 2024, 57, 6221−6232

$d^0_{K,z} = \sqrt{C_{n=N_K} N_K l_0^2/3} = \sqrt{1.75 \times 38 \times (0.96a)^2/3} = 4.5a$. As a result, the strand is stretched by a factor $d_{K,z}/d^0_{K,z} = 5.4$. This prediction of the geometric argument agrees well with $\lambda^\beta = 5.4 \pm 0.2$ in the simulations, confirming the role of the entanglement network in determining the draw ratio of necked polymers.

**4.4. Effects of Film Thickness.** Experiments have shown that the dilution of polymer entanglements due to nanoconfinement tends to promote brittle failure of ultrathin films.[12,14] Such an effect is not present here as the film thickness is larger than the unperturbed average end-to-end chain size $R_{ee}$, which is $28.8a$ for $N = 500$ in the simulations and 28 nm for the PS in the experiment.

Additional simulations with thicknesses of $48.0a$ and $186.9a$, which are half and twice the thickness in Figure 4, but still larger than $R_{ee}$, consistently reproduce ductile necking. Figures 7 and 8

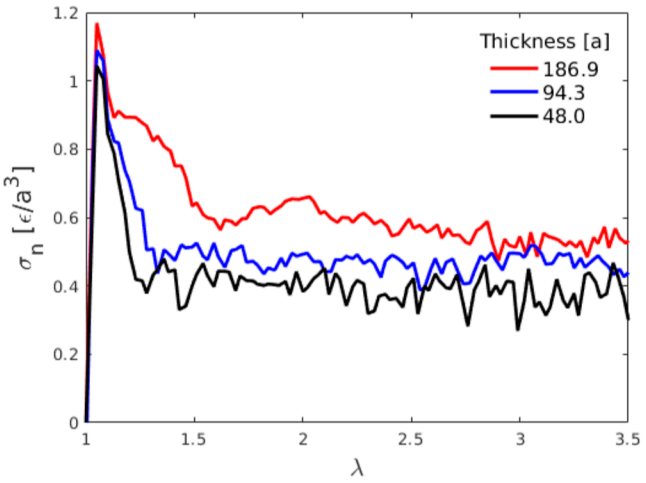


**Figure 7.** Nominal stress $\sigma_n$ as a function of the stretch ratio $\lambda$ for the thin film samples with indicated thicknesses.

show the stress–stretch curves and the morphologies of the necked thin films with thicknesses of $48.0a$ and $186.9a$. A ductile necking is observed, as indicated by the plateau of the stress–stretch curve in Figure 7 and the neck profile in Figure 8. The film thickness profiles in Figure 7 are fit to the hyperbolic tangent function $h(z) = \Delta h \tanh[(z - z_0)/w] + h_0$. For the thickness of $48.0a$, the fitting results are $\Delta h = -(16.5 \pm 0.1)a$, $z_0 = (205.9 \pm 0.2)a$, $w = (17.7 \pm 0.4)a$, and $h_0 = (27.2 \pm 0.1)a$. For thickness $186.9a$, the fitting results are $\Delta h = -(59.2 \pm 0.5)a$, $z_0 = (151.6 \pm 0.7)a$, $w = (79.8 \pm 1.3)a$, and $h_0 = (98.3 \pm 0.4)a$. The best fit results are indicated by the red lines in Figure 8c,d. In both cases, the neck width $2w$ is much larger than the entanglement spacing $d_e = 8a$. As the film thickness increases, the stress level for stable necking (including both the yield stress $\sigma_Y$ and the plateau stress $\sigma_P$) is raised, and the neck becomes broader. Understanding these trends is an interesting topic for future study. In all simulations, the simulation box size in the periodic $z$-direction for film stretching is sufficiently long to accommodate the coexistence of the thick $\alpha$ region and the necked $\beta$ region with broad necks. However, a much larger box size in the $z$-direction would be needed to reproduce multiple stable neck propagation processes simultaneously (see Figure 3a).

**4.5. Effects of Temperature.** Enhanced monomer mobility has been argued as an origin of ductility as temperature $T$ approaches $T_g$.[6,14] To clarify the role of monomer mobility, additional simulations of necking at elevated $T$ toward $T_g$ are performed. Figure 9a shows the nominal tensile stress $\sigma_n$ as a function of the stretch ratio $\lambda$ for the thin film necking at $T = 0.1\epsilon/k_B$, $0.15\epsilon/k_B$, $0.2\epsilon/k_B$, $0.25\epsilon/k_B$, and $0.3\epsilon/k_B$. The simulation sample used is that in Figure 4. Qualitatively, the same features are observed in the stress–stretch curves at different temperatures: a yield peak $\sigma_Y$ that corresponds to the initiation of the necked $\beta$ region and a subsequent plateau $\sigma_P$ at which the neck propagates steadily throughout the film. Quantitatively, Figure 9b shows $\sigma_Y$ and $\sigma_P$ decreases linearly with temperature for $T = 0.1\epsilon/k_B$, $0.15\epsilon/k_B$, $0.2\epsilon/k_B$, and $0.25\epsilon/k_B$. The linear dependence indicates that the stress level in the mechanical response involves a thermal agitation process, which may be theoretically described by the Eyring model. The linear temperature dependence also agrees with the values in the shear yielding and craze formation in bulk polymer glasses. The results for $T = 0.3\epsilon/k_B$ deviate from the linear dependence, as the temperature is close to $T_g$. Apart from the stress–stretch behavior, the morphology of the necked thin film at different temperatures is also analyzed. Figure 10 shows the thickness and density profiles for the coexistence of the thick $\alpha$ region and the necked $\beta$ region at different temperatures. Unlike the stress level, the average density $\rho^\beta$ and the average film thickness $h^\beta$ of the necked $\beta$ region depend on the temperature weakly. See Table 1 for a list of the values of $\rho^\beta$ and $h^\beta$. The simulations at different temperatures demonstrate the ductility of a glassy thin film in a broad temperature range below $T_g$.

With increasing $T$, the monomer mobility is enhanced, as measured by the $T$-dependence of the mean-square monomer displacement $\langle \Delta \vec{r}^2 \rangle$ at the deformation-relevant time scale (see Figure S6). Nevertheless, $\langle \Delta \vec{r}^2 \rangle$ is much smaller than the displacement induced by the plastic deformation and thus does not play a significant role in the ductility of the deformed films. Further analysis shows that the layers near the surfaces are more mobile but constitute a small fraction of the film and cause an insignificant effect.

**4.6. Effects of the Deformation Rate.** Another factor affecting the mechanics of thin film necking is the deformation rate. To examine the effects of the stretching velocity $v$, simulations with different values of $v$ with respect to $v_0 = 0.04a/\tau$ were performed. Figure 11a shows $\sigma_n$ as a function of $\lambda$ for the necking of the thin film in Figure 4 with deformation rates in the range $0.25 < v/v_0 < 4$. All deformation rates used are much higher compared with the limited monomer mobility at $T = 0.1\epsilon/k_B$ (see Figure S6). The stress–stretch curves exhibit a weak dependence on the deformation rates. Figure 11b shows that the yield stress $\sigma_Y$ increases linearly with the logarithm of $v/v_0$, in agreement with the Eyring model for yield. The plateau stress $\sigma_P$ decreases linearly with the logarithm of $v/v_o$ before leveling off at the highest deformation rate. The trends for the stress level are related to the morphology changes with increasing $v/v_o$. As shown by the thickness and density profiles in Figure 12 and the corresponding values $h^\beta$ and $\rho^\beta$ in Table 2, there are two major changes with increasing $v/v_o$: one is the emergence of more than one places for the initial strain localization (later only one develops into a stable neck propagation) and the other is the reduction in $h^\beta$ and $\rho^\beta$. As $v/v_0$ increases, a higher $\sigma_Y$ is needed to initiate necking, causing multiple sites of strain localization as well as more cavitation in


https://doi.org/10.1021/acs.macromol.4c00656
Macromolecules 2024, 57, 6221–6232

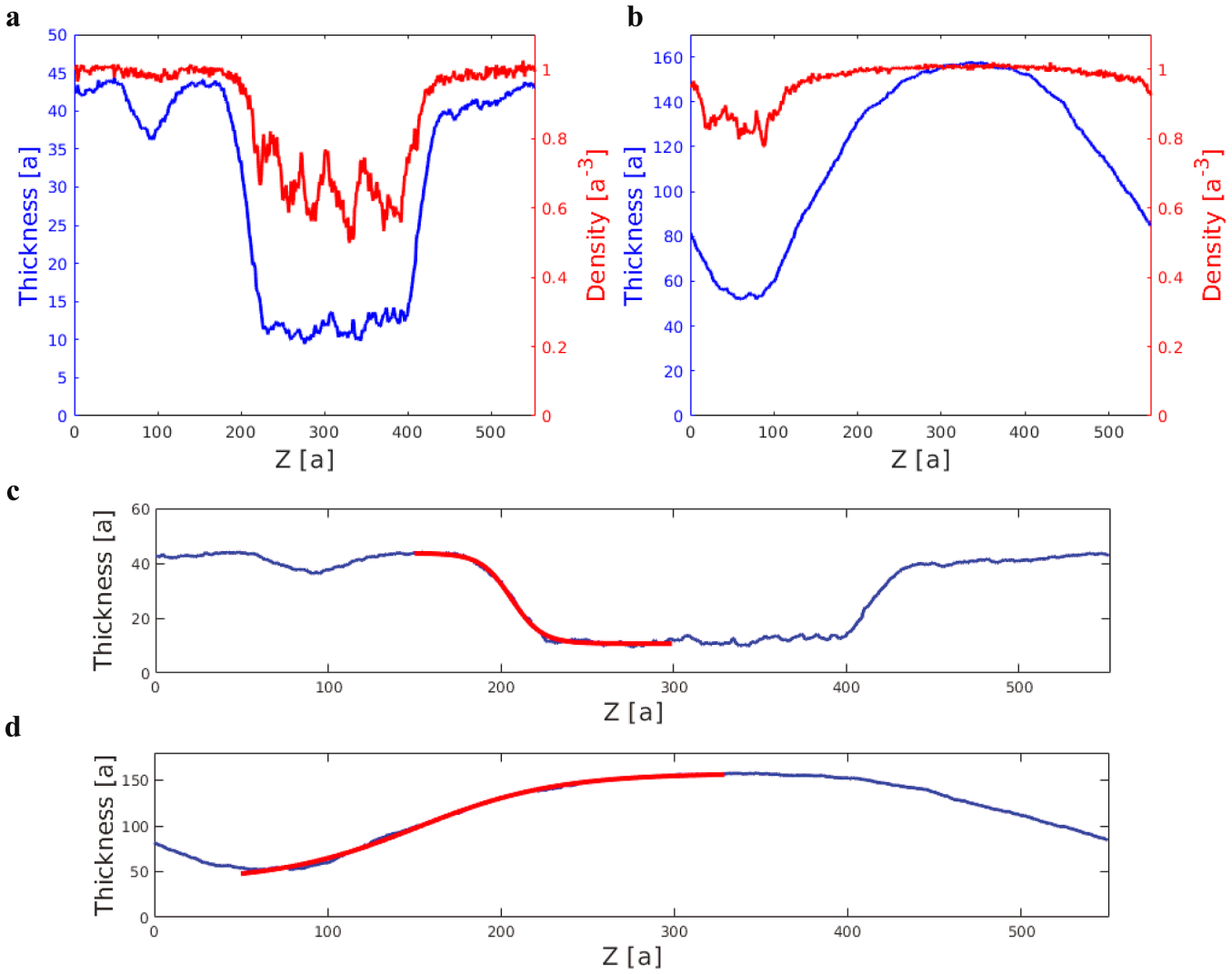


**Figure 8.** Thickness profiles and density profiles for the thin film samples with undeformed thicknesses (a) 48.0$a$ and (b) 186.9$a$. The best fits of the thickness profiles to the hyperbolic tangent function are indicated by the red lines in (c,d).

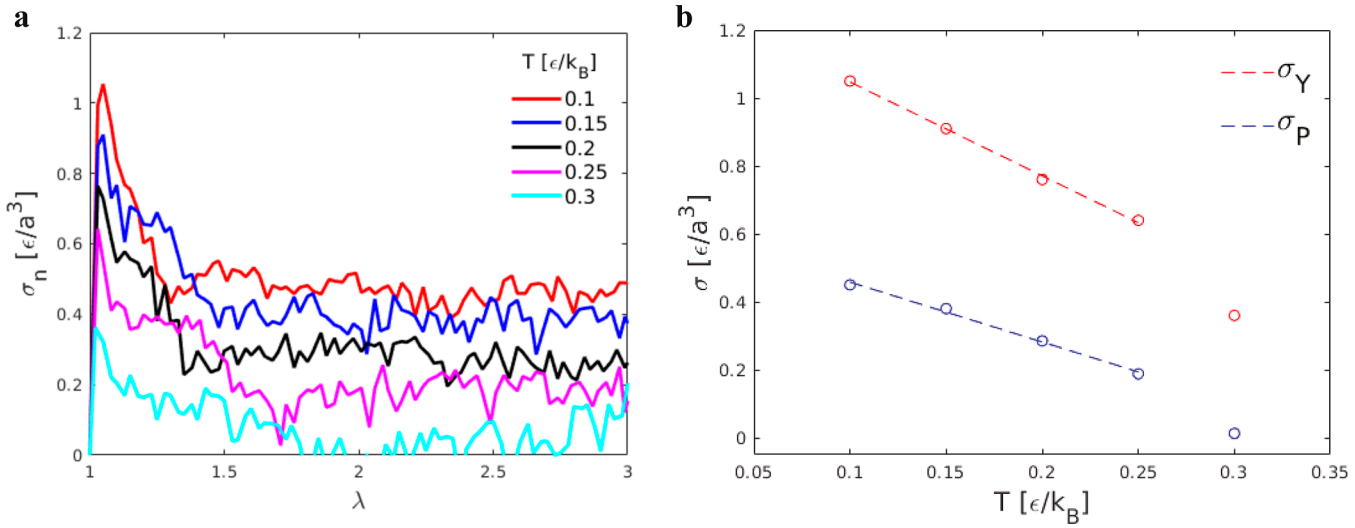


**Figure 9.** (a) Nominal stress $\sigma_n$ as a function of the stretch ratio $\lambda$ for thin film necking at different temperatures. (b) Yield stress $\sigma_Y$ and the plateau stress $\sigma_P$ as functions of temperature $T$. $\sigma_P$ is the average stress for $2 < \lambda < 2.5$. Dashed lines indicate the best fits to linear functions.

the necked region. Meanwhile, a lower nominal $\sigma_P$ is needed to stabilize a more perforated $\beta$ region with a reduced $\rho^\beta$. This set of simulations justifies using $v_0 = 0.04a/\tau$, which is in the range where the stress level depends weakly on the logarithm of the



https://doi.org/10.1021/acs.macromol.4c00656
Macromolecules 2024, 57, 6221−6232

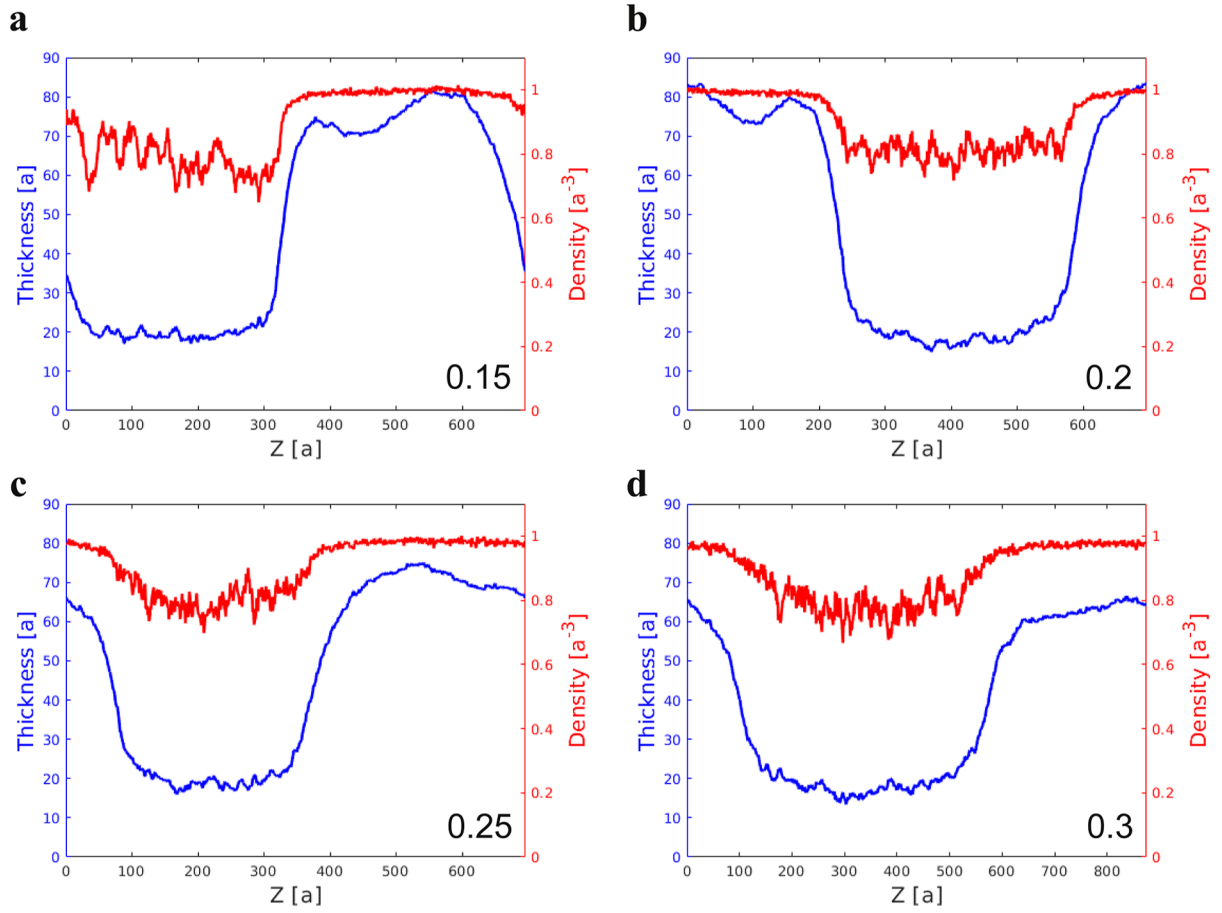


**Figure 10.** Thickness profiles and density profiles of thin film necking at indicated temperatures (unit: $\varepsilon/k_B$).

**Table 1. Average Density $\rho^\beta$ and Average Thickness $h^\beta$ of the Necked Region at Indicated Temperature $T$ and Stretch Ratio $\lambda$[a]**

| $T(\varepsilon/k_B)$ | $\lambda$ | range of $z(a)$ | $\rho^\beta(a^{-3})$ | $h^\beta(a)$ |
|---|---|---|---|---|
| 0.1 | 2.0 | 100−200 | 0.71 | 20.2 |
| 0.15 | 2.0 | 100−200 | 0.79 | 19.2 |
| 0.2 | 2.0 | 350−450 | 0.80 | 17.4 |
| 0.25 | 2.0 | 150−250 | 0.78 | 18.5 |
| 0.3 | 2.0 | 300−400 | 0.76 | 16.6 |

[a] $\rho^\beta$ and $h^\beta$ are the averages of the data in the indicated range of $z$-coordinate.

deformation rate but away from the high-rate regime with multiple places of strain localization and more cavitation.

## 5. CONCLUDING REMARKS

The large-scale molecular simulations have reproduced ductile thin film necking, as seen in experiments. Simulations of varying film thicknesses and temperatures have further demonstrated that a glassy polymer thin film may exhibit ductility through necking without the assistance of shifted $T_g$ or enhanced surface monomer mobility. However, the simulations cannot rule out the effects of $T_g$ and surface monomer mobility in ultrathin films. The thin films in the simulations do not correspond to ultrathin films, where the surface layers dominate the thin film response because the film thickness is comparable to or smaller than the average polymer chain size in the undeformed state.

It is not facile to establish the simulation protocols for reproducing the experimentally observed necking process in thin films made of polymers that are brittle in bulk, as the large-scale simulation contains $O(10^6)$ coarse-grained beads and the values of many control parameters need to be carefully selected. The protocols in this work properly separate the ductile deformation mode from the effects of nanoconfinement and the shift of the glass transition temperature with appropriately chosen deformation rate, allowing the demonstration of the ductility arising from the entanglement network and plane stress condition. Future simulations of glassy thin film mechanics can go beyond the generic coarse-grained polymer model and apply a scale-bridging approach to simulate chemically specific polymers such as PS.[47]

Using the large-scale molecular simulations, the microscopic details of the ductile thin film necking process that are experimentally hard to study are uncovered. These details include the morphological changes quantified by the film thickness and density profiles, local strain and stress distributions, and evolutions of chain conformations and entanglements. As a result, a clear microscopic picture of ductile thin film necking is depicted with numerical details, providing new and rich microscopic knowledge regarding the necking process.

The microscopic picture revealed is summarized as follows: An entanglement network is required to arrest the catastrophic chain pullout and support stable neck propagation by forcing the entangled chains to follow the neck profile. Entanglements orient the polymer chains and lead to sufficient strain hardening


https://doi.org/10.1021/acs.macromol.4c00656
Macromolecules 2024, 57, 6221−6232

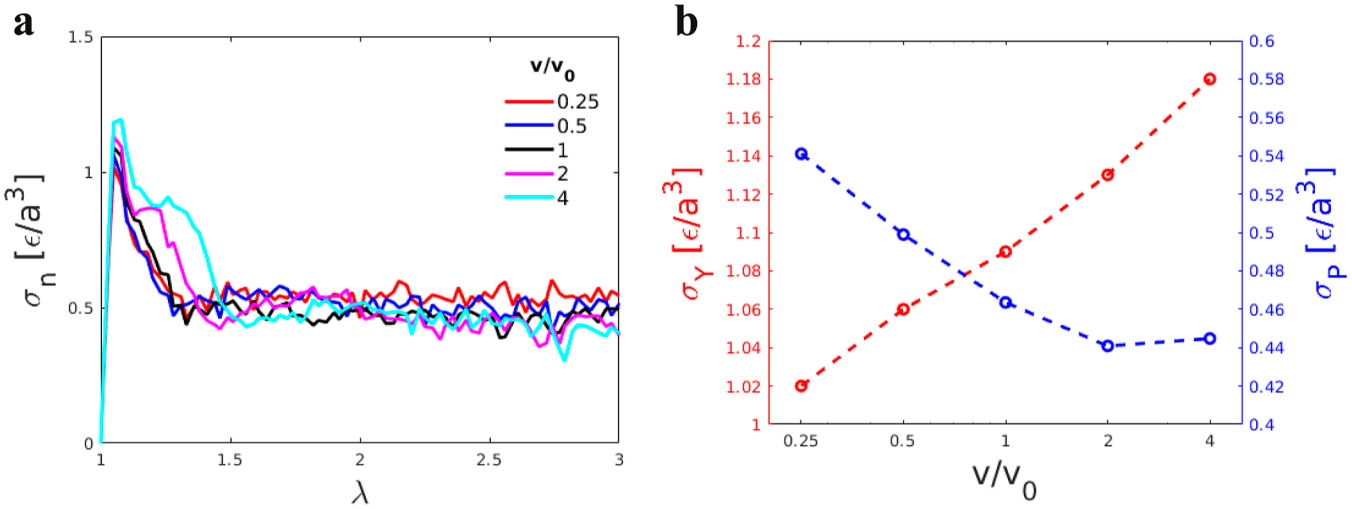


**Figure 11.** (a) Nominal stress $\sigma_n$ as a function of the stretch ratio $\lambda$ for thin film necking at different stretching velocities $v$ with respect to $v_0 = 0.04a/\tau$. (b) Yield stress $\sigma_Y$ and the plateau stress $\sigma_P$ as functions of $v/v_0$ on the logarithmic scale. $\sigma_P$ is the average stress for $2 < \lambda < 2.5$.

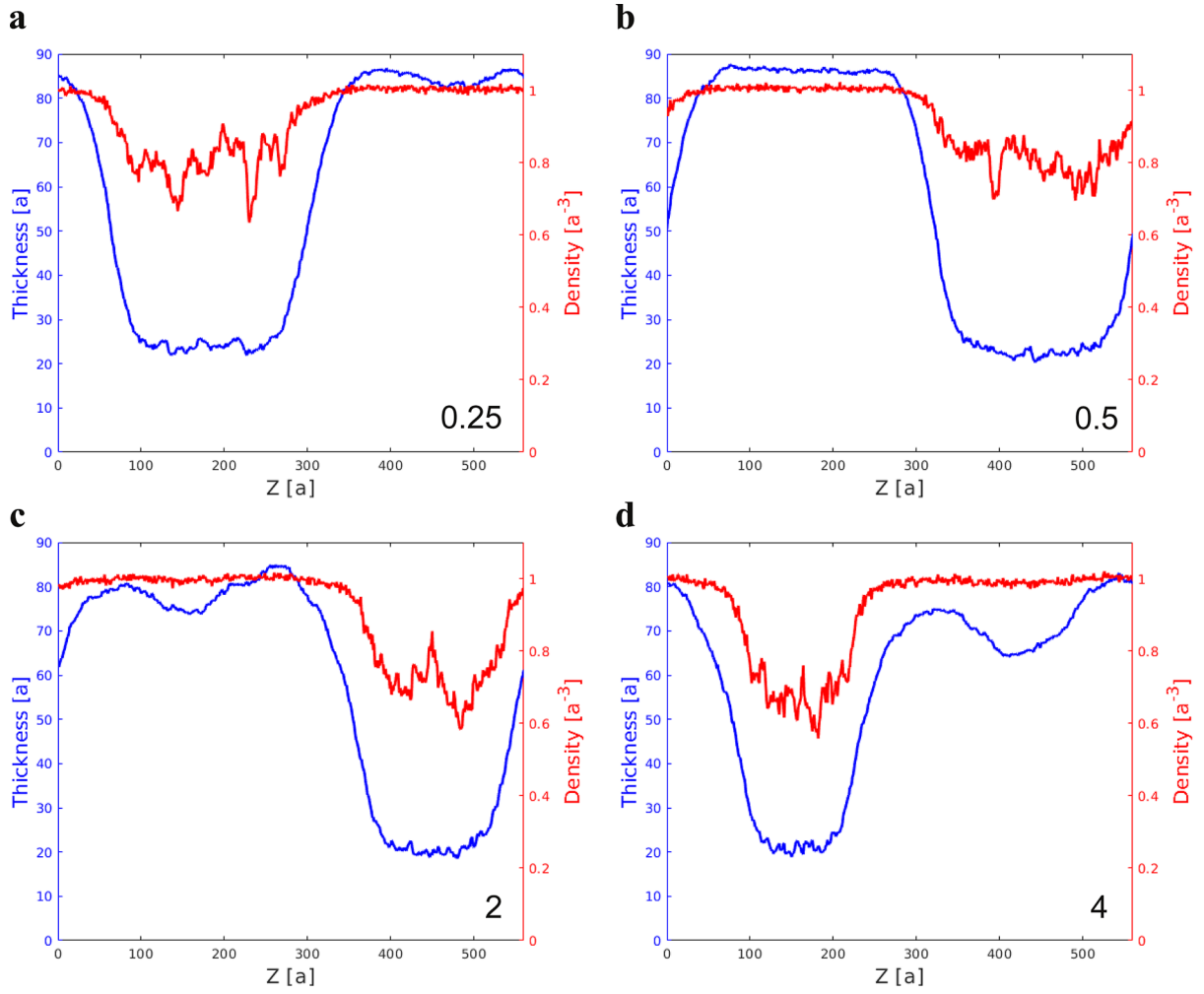


**Figure 12.** Thickness profiles and density profiles of thin film necking at indicated $v/v_0$.

that increases the local stress, which matches the reduced film thickness to maintain a constant tensile force without breaking any bonds. Despite the critical role of entanglements, the width of the neck is much larger than the entanglement spacing. The Considère construction predicts well the onset of necking but not the draw ratio of necked polymers, where voids break down the conservation of volume. Krupenkin and Fredrickson's geometric argument based on the extension of entanglement network strands works well in predicting the draw ratio.



https://doi.org/10.1021/acs.macromol.4c00656
Macromolecules 2024, 57, 6221−6232

Table 2. Average Density $\rho^{\beta}$ and Average Thickness $h^{\beta}$ of the Necked Region at Indicated $v/v_0$ and Stretch Ratio $\lambda$[a]

| $v/v_0$ | $\lambda$ | range of $z(a)$ | $\rho^{\beta}(a^{-3})$ | $h^{\beta}(a)$ |
|---|---|---|---|---|
| 0.25 | 1.5 | 120−220 | 0.79 | 24.1 |
| 0.5 | 1.5 | 400−500 | 0.80 | 22.2 |
| 1 | 1.5 | 100−200 | 0.75 | 21.8 |
| 2 | 1.5 | 400−500 | 0.70 | 20.4 |
| 4 | 1.5 | 120−180 | 0.66 | 21.0 |

[a] $\rho^{\beta}$ and $h^{\beta}$ are the averages of the data in the indicated range of $z$-coordinate.

It is anticipated that this simulation work would stimulate the development of a micromechanics model of polymer thin film necking. Specifically, the finding that the strain hardening in the necked region supports stable neck propagation may motivate the revision of the existing necking model that assumes the polymer acts as a Newtonian fluid under deformation.[48] The strain-hardening physics of entangled glassy polymers[50] may be properly incorporated into the necking model. It is also anticipated that the findings presented here may promote the molecular design of stretchable and durable polymer thin films for their applications in many engineering fields. The micromechanics may be integrated with continuum mechanics of deformation and fracture to enable a scale-bridging design of thin film mechanics. Additionally, the work is also of interest to the researchers using cold drawing to produce ductile polymer fibers with reduced diameters.[51−53]

## ■ ASSOCIATED CONTENT

### Supporting Information

The Supporting Information is available free of charge at https://pubs.acs.org/doi/10.1021/acs.macromol.4c00656.

Quenching simulation and glass transition; atomic shear strain; simulations of strain hardening in bulk samples; simulations of crazing; neck width analysis; bond length statistics; and monomer mobility (PDF)

Side profiles of the thin films of chain length $N$ = 500 during necking for $M$ = 1800 (MP4)

Side profiles of the thin films of chain length $N$ = 500 during necking for $M$ = 3600 (MP4)

Side profiles of the bulk sample of chain length $N$ = 500 during crazing for $M$ = 1800 (MP4)

## ■ AUTHOR INFORMATION


### Corresponding Author

**Ting Ge** − *Department of Chemistry and Biochemistry, University of South Carolina, Columbia, South Carolina 29208, United States;* orcid.org/0000-0003-2456-732X; Email: tingg@mailbox.sc.edu

### Authors

**Siteng Zhang** − *Department of Chemistry and Biochemistry, University of South Carolina, Columbia, South Carolina 29208, United States*

**Zhiqiang Cao** − *School of Polymer Science and Engineering, Center for Optoelectronic Materials and Device, The University of Southern Mississippi, Hattiesburg, Mississippi 39406, United States*

**Xiaodan Gu** − *School of Polymer Science and Engineering, Center for Optoelectronic Materials and Device, The University of Southern Mississippi, Hattiesburg, Mississippi 39406, United States;* orcid.org/0000-0002-1123-3673

Complete contact information is available at: https://pubs.acs.org/10.1021/acs.macromol.4c00656


### Notes

The authors declare no competing financial interest.

## ■ ACKNOWLEDGMENTS

We thank S. Q. Wang for helpful discussions. X.G. thanks the National Science Foundation under award number DMR-2047689 for supporting the thin-film mechanics experimental characterization in this work. T.G. acknowledges start-up funds from the University of South Carolina and the National Science Foundation CAREER award DMR-2236693. Computational resources were provided by the University of South Carolina's flagship computing cluster Hyperion.

## ■ REFERENCES


(1) Jones, R. L.; Kumar, S. K.; Ho, D. L.; Briber, R. M.; Russell, T. P. Chain conformation in ultrathin polymer films using small-angle neutron scattering. *Macromolecules* **2001**, *34*, 559−567.

(2) Si, L.; Massa, M. V.; Dalnoki-Veress, K.; Brown, H. R.; Jones, R. A. L. Chain entanglement in thin freestanding polymer films. *Phys. Rev. Lett.* **2005**, *94*, 127801.

(3) McGraw, J. D.; Salez, T.; Bäumchen, O.; Raphaël, E.; Dalnoki-Veress, K. Self-similarity and energy dissipation in stepped polymer films. *Phys. Rev. Lett.* **2012**, *109*, 128303.

(4) Ismail, A. F.; Padaki, M.; Hilal, N.; Matsuura, T.; Lau, W. J. Thin film composite membrane - Recent development and future potential. *Desalination* **2015**, *356*, 140−148.

(5) Liu, Y.; Chen, Y. C.; Hutchens, S.; Lawrence, J.; Emrick, T.; Crosby, A. J. Directly Measuring the Complete Stress-Strain Response of Ultrathin Polymer Films. *Macromolecules* **2015**, *48*, 6534−6540.

(6) Bay, R. K.; Shimomura, S.; Liu, Y.; Ilton, M.; Crosby, A. J. Confinement Effect on Strain Localizations in Glassy Polymer Films. *Macromolecules* **2018**, *51*, 3647−3653.

(7) Wang, S.; Xu, J.; Wang, W.; Wang, G. J. N.; Rastak, R.; Molina-Lopez, F.; Chung, J. W.; Niu, S.; Feig, V. R.; Lopez, J.; et al. Skin electronics from scalable fabrication of an intrinsically stretchable transistor array. *Nature* **2018**, *555*, 83−88.

(8) Gu, X.; Shaw, L.; Gu, K.; Toney, M. F.; Bao, Z. The meniscus-guided deposition of semiconducting polymers. *Nat. Commun.* **2018**, *9*, 534.

(9) Zhang, S.; Ocheje, M. U.; Luo, S.; Ehlenberg, D.; Appleby, B.; Weller, D.; Zhou, D.; Rondeau-Gagné, S.; Gu, X. Probing the Viscoelastic Property of Pseudo Free-Standing Conjugated Polymeric Thin Films. *Macromol. Rapid Commun.* **2018**, *39*, 1−8.

(10) Ito, M. M.; Gibbons, A. H.; Qin, D.; Yamamoto, D.; Jiang, H.; Yamaguchi, D.; Tanaka, K.; Sivaniah, E. Structural colour using organized microfibrillation in glassy polymer films. *Nature* **2019**, *570*, 363−367.

(11) Weller, D. W.; Ma, G.; Galuska, L. A.; Zhang, S.; Stringer, M.; Aracri, S.; Wang, W.; Hong, K.; Gu, X. Strain-Induced Nanocavitation in Block Copolymer Thin Films for High Performance Filtration Membranes. *ACS Appl. Polym. Mater.* **2021**, *3*, 5666−5673.

(12) Zhang, S.; Koizumi, M.; Cao, Z.; Mao, K. S.; Qian, Z.; Galuska, L. A.; Jin, L.; Gu, X. Directly Probing the Fracture Behavior of Ultrathin Polymeric Films. *ACS Polym. Au* **2021**, *1*, 16−29.

(13) Zhang, S.; Galuska, L. A.; Gu, X. Water-assisted mechanical testing of polymeric thin-films. *J. Polym. Sci.* **2022**, *60*, 1108−1129.

(14) Bay, R. K.; Zhang, T.; Shimomura, S.; Ilton, M.; Tanaka, K.; Riggleman, R. A.; Crosby, A. J. Decoupling the Impact of Entanglements and Mobility on the Failure Properties of Ultrathin Polymer Films. *Macromolecules* **2022**, *55*, 8505−8513.

(15) Haward, R. N.; Young, R. *The Physics of Glassy Polymers*; Springer: Netherlands, 1997; .

(16) Ward, I. M.; Sweeney, J. *Mechanical Properties of Solid Polymers*; John Wiley & Sons Ltd: New York, 2013; .

(17) Li, X.; Wang, S. Q. Mapping Brittle and Ductile Behaviors of Polymeric Glasses under Large Extension. *ACS Macro Lett.* **2015**, *4*, 1110−1113.
(18) Liu, J.; Lin, P.; Cheng, S.; Wang, W.; Mays, J. W.; Wang, S. Q. Polystyrene Glasses under Compression: Ductile and Brittle Responses. *ACS Macro Lett.* **2015**, *4*, 1072−1076.
(19) Roth, C. B. *Polymer Glasses*; CRC Press, 2016; .
(20) Liu, J.; Zhao, Z.; Wang, W.; Mays, J. W.; Wang, S. Q. Brittle-ductile transition in uniaxial compression of polymer glasses. *J. Polym. Sci., Part B: Polym. Phys.* **2019**, *57*, 758−770.
(21) Rottler, J.; Barsky, S.; Robbins, M. O. Cracks and Crazes: On Calculating the Macroscopic Fracture Energy of Glassy Polymers from Molecular Simulations. *Phys. Rev. Lett.* **2002**, *89*, 148304.
(22) Rottler, J.; Robbins, M. O. Jamming under Tension in Polymer Crazes. *Phys. Rev. Lett.* **2002**, *89*, 195501−195508.
(23) Rottler, J.; Robbins, M. O. Unified description of aging and rate effects in yield of glassy solids. *Phys. Rev. Lett.* **2005**, *95*, 225504−225505.
(24) Riggleman, R. A.; Yoshimoto, K.; Douglas, J. F.; De Pablo, J. J. Influence of confinement on the fragility of antiplasticized and pure polymer films. *Phys. Rev. Lett.* **2006**, *97*, 045502−045504.
(25) Riggleman, R. A.; Lee, H.-N.; Ediger, M. D.; De Pablo, J. J. Free volume and finite-size effects in a polymer glass under stress. *Phys. Rev. Lett.* **2007**, *99*, 215501.
(26) Hoy, R. S.; Robbins, M. O. Strain hardening in polymer glasses: Limitations of network models. *Phys. Rev. Lett.* **2007**, *99*, 117801−117804.
(27) Warren, M.; Rottler, J. Microscopic view of accelerated dynamics in deformed polymer glasses. *Phys. Rev. Lett.* **2010**, *104*, 205501−205504.
(28) Ge, T.; Robbins, M. O. Anisotropic Plasticity and Chain Orientation in Polymer Glasses. *J. Polym. Sci., Part B: Polym. Phys.* **2010**, *48*, 1473−1482.
(29) Ge, T.; Pierce, F.; Perahia, D.; Grest, G. S.; Robbins, M. O. Molecular dynamics simulations of polymer welding: Strength from interfacial entanglements. *Phys. Rev. Lett.* **2013**, *110*, 098301.
(30) Ge, T.; Grest, G. S.; Robbins, M. O. Structure and strength at immiscible polymer interfaces. *ACS Macro Lett.* **2013**, *2*, 882−886.
(31) Shavit, A.; Riggleman, R. A. Strain localization in glassy polymers under cylindrical confinement. *Phys. Chem. Chem. Phys.* **2014**, *16*, 10301−10309.
(32) Jabbari-Farouji, S.; Lame, O.; Perez, M.; Rottler, J.; Barrat, J. L. Role of the Intercrystalline Tie Chains Network in the Mechanical Response of Semicrystalline Polymers. *Phys. Rev. Lett.* **2017**, *118*, 217802−217805.
(33) Wang, J.; Ge, T. Crazing Reveals an Entanglement Network in Glassy Ring Polymers. *Macromolecules* **2021**, *54*, 7500−7511.
(34) Yang, E.; Riggleman, R. A. Role of Local Structure in the Enhanced Dynamics of Deformed Glasses. *Phys. Rev. Lett.* **2022**, *128*, 097801.
(35) Dietz, J. D.; Nan, K.; Hoy, R. S. Unexpected Ductility in Semiflexible Polymer Glasses with Entanglement Length Equal to their Kuhn Length. *Phys. Rev. Lett.* **2022**, *129*, 127801.
(36) Kremer, K.; Grest, G. S. Dynamics of entangled linear polymer melts: A molecular-dynamics simulation. *J. Chem. Phys.* **1990**, *92*, 5057−5086.
(37) Hoy, R. S.; Foteinopoulou, K.; Kröger, M. Topological analysis of polymeric melts: Chain-length effects and fast-converging estimators for entanglement length. *Phys. Rev. E* **2009**, *80*, 031803.
(38) Kröger, M.; Dietz, J. D.; Hoy, R. S.; Luap, C. The Z1+ package: Shortest multiple disconnected path for the analysis of entanglements in macromolecular systems. *Comput. Phys. Commun.* **2023**, *283*, 108567.
(39) Everaers, R.; Karimi-Varzaneh, H. A.; Fleck, F.; Hojdis, N.; Svaneborg, C. Kremer Grest Models for Commodity Polymer Melts: Linking Theory, Experiment, and Simulation at the Kuhn Scale. *Macromolecules* **2020**, *53*, 1901−1916.
(40) Sides, S. W.; Grest, G. S.; Stevens, M. J.; Plimpton, S. J. Effect of End-Tethered Polymers on Surface Adhesion of Glassy Polymers. *J. Polym. Sci., Part B: Polym. Phys.* **2004**, *42*, 199−208.
(41) Thompson, A. P.; Aktulga, H. M.; Berger, R.; Bolintineanu, D. S.; Brown, W. M.; Crozier, P. S.; in 't Veld, P. J.; Kohlmeyer, A.; Moore, S. G.; Nguyen, T. D.; Shan, R.; Stevens, M. J.; Tranchida, J.; Trott, C.; Plimpton, S. J. LAMMPS-a flexible simulation tool for particle-based materials modeling at the atomic, meso, and continuum scales. *Comput. Phys. Commun.* **2022**, *271*, 108171.
(42) Rottler, J.; Robbins, M. O. Growth, microstructure, and failure of crazes in glassy polymers. *Phys. Rev. E* **2003**, *68*, 011801.
(43) Zhang, S.; Ocheje, M. U.; Luo, S.; Ehlenberg, D.; Appleby, B.; Weller, D.; Zhou, D.; Rondeau-Gagné, S.; Gu, X. Probing the Viscoelastic Property of Pseudo Free-Standing Conjugated Polymeric Thin Films. *Macromol. Rapid Commun.* **2018**, *39*, 1800092.
(44) Kramer, E. J. Microscopic and Molecular Fundamentals of Crazing. *Adv. Polym. Sci.* **1983**, *52*, 1−56.
(45) Kramer, E. J.; Berger, L. L. Fundamental Processes of Craze Growth and Fracture. *Adv. Polym. Sci.* **1990**, *91−92*, 1−68.
(46) Ge, T.; Tzoumanekas, C.; Anogiannakis, S. D.; Hoy, R. S.; Robbins, M. O. Entanglements in glassy polymer crazing: Cross-links or tubes? *Macromolecules* **2017**, *50*, 459−471.
(47) Wang, J.; in 't Veld, P. J.; Robbins, M. O.; Ge, T. Effects of Coarse-Graining on Molecular Simulation of Craze Formation in Polymer Glass. *Macromolecules* **2022**, *55*, 1267−1278.
(48) Krupenkin, T. N.; Fredrickson, G. H. Crazing in two and three dimensions. 2. Three-dimensional crazing. *Macromolecules* **1999**, *32*, 5036−5045.
(49) Stevens, M. J. Interfacial fracture between highly cross-linked polymer networks and a solid surface: effect of interfacial bond density. *Macromolecules* **2001**, *34*, 2710−2718.
(50) Chen, K.; Schweizer, K. S. Suppressed segmental relaxation as the origin of strain hardening in polymer glasses. *Phys. Rev. Lett.* **2009**, *102*, 038301.
(51) Kolluru, P. V.; Chasiotis, I. Interplay of molecular and specimen length scales in the large deformation mechanical behavior of polystyrene nanofibers. *Polymer* **2015**, *56*, 507−515.
(52) Kolluru, P. V.; Chasiotis, I. A master curve for the size and strain rate dependent large deformation behavior of PS nanofibers at room temperature. *Polymer* **2016**, *99*, 544−551.
(53) Shabahang, S.; Tao, G.; Kaufman, J. J.; Qiao, Y.; Wei, L.; Bouchenot, T.; Gordon, A. P.; Fink, Y.; Bai, Y.; Hoy, R. S.; Abouraddy, A. F. Controlled fragmentation of multimaterial fibres and films via polymer cold-drawing. *Nature* **2016**, *534*, 529−533.


https://doi.org/10.1021/acs.macromol.4c00656
*Macromolecules* 2024, 57, 6221−6232